Palaeogeography, Palaeoclimatology, Palaeoecology 276 (2009) 47–55

Contents lists available at ScienceDirect

Palaeogeography, Palaeoclimatology, Palaeoecology

journal homepage: www.elsevier.com/locate/palaeo

MoGroFunGen: A numerical model for reconstructing intra-annual growth rates of bivalve molluscs

David H. Goodwin [a,*], Prabasaj Paul [b], Christine L. Wissink [a]

[a] Department of Geosciences, Denison University, Granville Ohio 43023, United States
[b] Department of Physics and Astronomy, Denison University, Granville Ohio 43023, United States

ARTICLE INFO

Article history:
Received 23 July 2008
Received in revised form 12 February 2009
Accepted 21 February 2009

Keywords:
Modeling
Growth
Oxygen
Isotope
Bivalve
Mollusc

ABSTRACT

Bivalve mollusc shells contain valuable archives of biological and environmental information. For example, periodic microgrowth increments record intra-annual growth rates that vary, in large part, as a function of temperature. Unfortunately, these increments are often not preserved, or were deposited at equivocal intervals, especially in fossils or shells with obscure increments. Here we present a new numerical model that reconstructs intra-annual growth rates by relating linear growth and time using oxygen isotopes from shell carbonate. The model involves converting observed oxygen isotope values from shell carbonate ($\delta^{18}O_{carb}$) to temperatures, which requires knowledge of the oxygen isotope composition of water ($\delta^{18}O_{water}$). Then calculated temperatures are converted to dates using temporally calibrated temperature records. Next, dates are plotted versus sample distance (measured from sampled shells), fit with a monotonic cubic spline, and finally the first derivative of this function is evaluated yielding the growth function. The variance of this function is estimated through resampling by incorporating the uncertainty associated with $\delta^{18}O$ measurement (e.g., $\pm 0.08‰$). This numerical model produces a distribution of growth functions, from which we calculate the average growth function. Modeled growth functions agree well with independently derived growth functions, which suggests our modeling procedure produces reliable estimates of intra-annual growth rates. These data can, in turn, provide valuable ecological information, such as the timing of highest intra-annual growth rates, growth-limiting temperatures, and optimal growth temperatures. This final parameter is particularly important because optimal growth temperatures can now be estimated without any *a priori* knowledge of growth rates.

1. Introduction

The accretionary skeletons of bivalve molluscs are an important source of environmental, biological, and evolutionary information (Wefer and Berger, 1991; Jones and Gould, 1999; Richardson, 2001; Goodwin et al., 2008a). The rate and timing of growth are controlled by numerous factors: temperature (Jones et al., 1989; Schöne et al., 2002a), salinity (Koike, 1980), age (Jones et al., 1989), reproductive cycle (Sato, 1995), tidal cycle and intertidal position (Ohno, 1989; Goodwin et al., 2001), and nutrient availability (Coe, 1948; Schöne et al., 2003). Temperature, however, appears to be dominant among the factors controlling intra-annual growth rates of most species (Koike, 1980; Goodwin et al., 2001; Schöne et al., 2002a). Traditionally, counts and measurements of periodic microgrowth increments, often a function of the tidal cycle (Richardson, 2001), have been used to reconstruct temperature dependant intra-annual growth rates. Unfortunately, these increments are often not preserved, or were deposited at equivocal intervals, making this approach difficult, especially in fossil specimens.

Several recent studies have used oxygen isotope ($\delta^{18}O$) profiles to model bivalve mollusc shell growth. Ivany et al. (2003) used a best-fit sinusoid model, developed by Wilkinson and Ivany (2002) and later modified by De Ridder et al. (2007), to resolve average annual isotopic ratios, seasonal variation of isotopic ratios, and shell growth rates. De Ridder et al. (2004) developed a model to convert the distance scale to a time-scale by taking advantage of strong periodicity (likely annual) in observed $\delta^{18}O$ profiles. A similar approach was employed by Elliot et al. (2003), who used a modeling approach to stretch distance axes in order to compare geochemical profiles from multiple specimens. These studies demonstrate the utility of modeling approaches for understanding inter-annual growth of biogenic hard parts. Goodwin et al. (2003) modeled intra-annual shell growth to document various patterns of isotopic variation associated with senescence. This study, however, relied heavily on *a priori* knowledge of intra-annual growth rates based on increment width counts. To overcome this limitation, we present a novel mathematical method that relates shell growth and time using $\delta^{18}O$ variation to reconstruct *intra-annual* growth rates in bivalve molluscs.

The concept is straightforward: the first derivative of a function relating cumulative linear growth to time represents intra-annual growth rate—the growth function. In practice, this technique involves

* Corresponding author.
E-mail addresses: goodwind@denison.edu (D.H. Goodwin), paulp@denison.edu (P. Paul), clwissink@gmail.com (C.L. Wissink).

0031-0182/$ – see front matter © 2009 Elsevier B.V. All rights reserved.
doi:10.1016/j.palaeo.2009.02.026

converting observed oxygen isotope ratios from shell carbonate ($\delta^{18}O_{carb}$) to temperatures, which requires knowledge of the oxygen isotopic composition of water ($\delta^{18}O_{water}$). Then calculated temperatures are converted to dates using temporally calibrated temperature records. Next, dates are plotted versus sample distance (measured from sampled shells), and fit with a monotonic cubic spline. Finally, the first derivative of this function is evaluated. This procedure is then repeated by incorporating the uncertainty associated with $\delta^{18}O$ measurement (e.g., ±0.08‰). The numerical model produces a distribution of growth functions, from which the average growth function is calculated. These data can, in turn, provide valuable ecological information, such as the timing of highest intra-annual growth rates, growth-limiting temperatures, and optimal growth temperatures. This final parameter is particularly important because optimal growth temperatures can now be estimated without any *a priori* knowledge of growth rates.

2. Materials and methods

2.1. Specimens and environmental data

We applied our model to three specimens of *Chione* (*Chionista*) *cortezi* collected from the Colorado River delta in the northern Gulf of California. All specimens were collected alive: IP1-A1R was collected from Isla Pelicano (31° 45.7′ N, 114° 38.9′ W) in 1995, and IM11-A1L and IM11-A2L were collected from Isla Montague (31° 40.2′ N, 114° 41.4′ W) in 2000. Additional details on these localities are available in Goodwin et al. (2001) and Goodwin et al. (2003). The shells are housed in the CEAM research collection in the Department of Geosciences at the University of Arizona.

Specimens were sacrificed immediately after collection and the flesh was removed. In the lab, valves were sectioned along the dorso-ventral axis of maximum shell height, and thick sections were mounted on microscope slides. Carbonate samples, each with a mass between 50 and 100 μg, were drilled from the prismatic layer. We sampled the second year of growth from IP1-A1R and the third year from IM11-A1L and IM11-A2L. Isotopic analyses of carbonate from IP1-A1R were performed on a Finnigan MAT 252 mass spectrometer equipped with at Kiel III automated sampling devise. Samples from IM11-A1L and IM11-A2L were performed on a Micromass Optima IRMS with a common acid-bath autocarbonate device. Additional details on analytical procedures can be found in Goodwin et al. (2001) and Goodwin et al. (2003). Results are reported in δ notation (‰) by calibration to the NBS-19 reference standard ($\delta^{18}O = -2.20$‰ VPDB). Regardless of which machine was used, repeated analysis of laboratory standards resulted in standard deviations of ±0.08‰.

Microgrowth increment widths, which were deposited in response to the tidal cycle (Richardson, 2001), were measured from the same plane as the $\delta^{18}O$ samples. Thick sections were polished and then etched in a weak acid (Goodwin et al., 2001). This procedure results in differential dissolution of growth lines and growth increments *sensu* Richardson et al. (1981). Increments were photographed under inclined reflected light and widths were measured from digital images. The increment width profiles from IM11-A1L and IM11-A2L were directly dated by Goodwin et al. (2001). The increment width profile from IP1-A1R was roughly calibrated with time by centering it on the midpoint of the year (Goodwin et al., 2003).

Our temperature model is based on data recorded from the IM11 collection site (Goodwin et al., 2001). Temperatures were recorded every 2 h for a complete year (10:00 AM, February 16, 1999 to 10:00 AM, February 16 2000). Two loggers (HOBO® Temp: resolution and accuracy ~0.5 °C) were deployed and their respective records were significantly correlated ($r^2 = 0.995$, $p < 0.01$). Here we use average daily temperatures calculated from one of the two temperature records. Logger uncertainty was not included in the model.

2.2. MoGroFunGen: Explanation of the model

The model presented here, MoGroFunGen, or the Mollusc Growth Function Generator, is designed to extract intra-annual growth curves from bivalve mollusc shells. Our approach is similar theoretically to

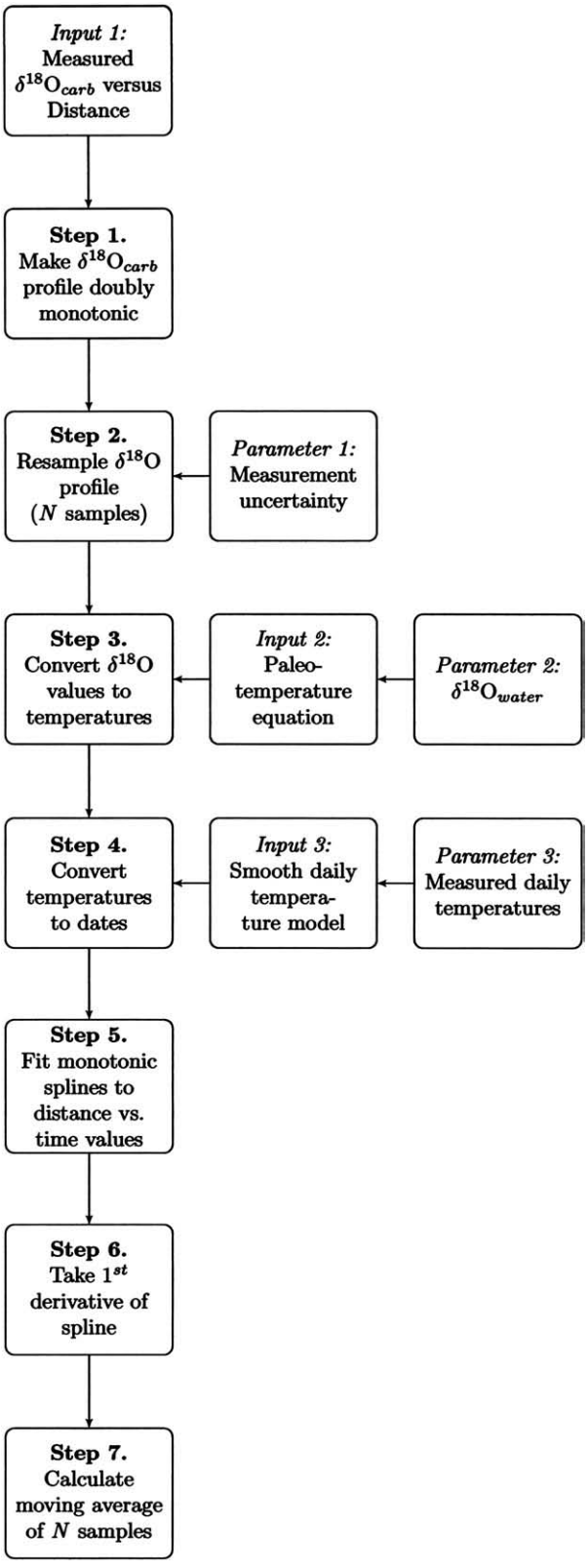

Fig. 1. Flow chart outlining the steps, inputs, and parameters used in the MoGroFunGen model.

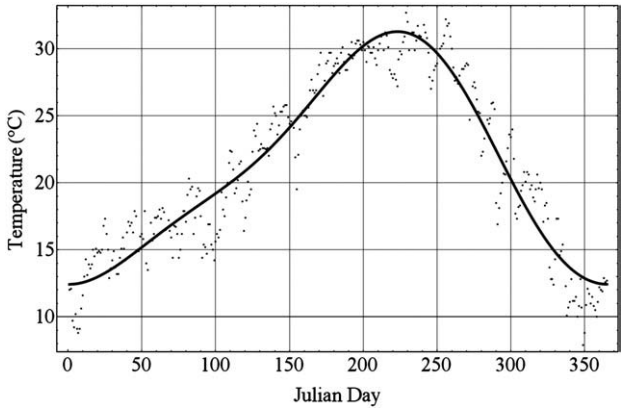

Fig. 2. Annual temperature model (*Parameter 3*). The dots show average daily temperatures. The solid line is the smooth daily temperature model (*Input 3*). See text for discussion.

the method devised by Schöne et al. (2002b). However, whereas they used growth rates to reconstruct sea-surface temperatures, here we use the relationship among temperature, $\delta^{18}O_{carb}$, and sample distance to reconstruct intra-annual growth rates. The model was implemented in Mathematica 6.0™, and the source code is available on request.

2.2.1. Parameters and Inputs

The model incorporates three *parameters*, three *inputs*, and involves seven steps (Fig. 1). *Parameter 1* is the uncertainty associated with repeated analysis of laboratory standards (here ±0.08‰). Parameter 2 is a static $\delta^{18}O_{water}$ value. We used a value of 0‰ based on observations from the northern Gulf of California (Goodwin et al., 2001). *Parameter 3* is average daily temperatures (°C) for a complete year (365 days) (Fig. 2).

The first input (*Input 1*) consists of measured $\delta^{18}O_{carb}$ values from a single year of shell growth and the cumulative distance (μm) between sample holes (Fig. 3; Appendix A). *Input 2* is a paleotemperature equation. Here we used Eq. (1) from Grossman and Ku (1986):

$$T(^{\circ}C) = 20.6 - 4.34\left(\delta^{18}O_{carb} - \left(\delta^{18}O_{water} - 0.2\right)\right). \quad (1)$$

This equation suggests that each 4.34 °C change in temperature results in a one permil shift in shell carbonate. Finally, *Input 3* is a smooth daily temperature model derived from *Parameter 3*. The smooth daily temperature model has two monotonic intervals: an increasing interval from the coldest to the hottest day of the year (spring), and a decreasing interval from the hottest to the coldest day of the year (autumn) (Fig. 2). Smoothing is carried out by expressing the temperature profile as a Fourier series and then retaining the 0th (average), 1st and 2nd harmonics. While truncating the series after the 1st harmonic results in an unambiguously doubly monotonic sinusoid, it fails to capture the significant asymmetry present in many temperature profiles. The resulting function implies that no more than two values of time correspond to each temperature value, one in spring and one in autumn.

2.2.2. Modeling procedures

In the first step of the model (Fig. 1), we ensure that the $\delta^{18}O_{carb}$ profile has two monotonic intervals—a decreasing interval (increasing temperature) and an increasing interval (decreasing temperature)—by culling points from the measured $\delta^{18}O_{carb}$ versus distance data set (Fig. 3). We use the most negative $\delta^{18}O$ value, which represents the hottest part of the summer, to separate the two intervals. Then successive $\delta^{18}O_{carb}$ values in each interval are compared and samples that result in monotonic trends are retained (Fig. 3). The model produces similar output regardless of which points are discarded (see Section 4.2).

Next, the doubly monotonic $\delta^{18}O_{carb}$ profile is resampled to generate additional profiles (Step 2; Fig. 1). Given sampling error and precision error of the mass spectrometer (±0.08‰), it is assumed that the observed doubly monotonic $\delta^{18}O_{carb}$ profile is an estimate of the specimen's true isotopic profile. We therefore generated a distribution of estimated isotopic profiles by first assuming that each observed $\delta^{18}O_{carb}$ value is a mean estimate of a normal distribution of $\delta^{18}O_{carb}$ values for that particular interval of time, and then resampling from the distributions using a standard deviation of 0.08‰ (*parameter 1*; Fig. 1). A pseudorandom number generator was used to produce *N* data sets from these independent normal distributions. Each resulting data set, conceptually, is the possible result of a new measurement of carbonate from each drill hole. Resampled $\delta^{18}O_{carb}$ versus distance data sets that are not doubly monotonic are discarded, and the procedure is repeated until the desired number ($N = 50\,000$) is reached.

In Step 3, $\delta^{18}O_{carb}$ values from the resampled data sets are converted to temperatures using Eq. (1) (*Input 2*). This straightforward procedure, of course, requires knowledge of $\delta^{18}O_{water}$ values. Because the model is designed to be used with marine molluscs, we assume relatively little variation of the oxygen isotopic composition of sea water and, therefore, use a static $\delta^{18}O_{water}$ value (Goodwin et al., 2001). Future modifications of the model will incorporate dynamic $\delta^{18}O_{water}$ values (Goodwin et al., 2008b).

Step 4 involves converting temperatures to Julian dates (1–365) using the smooth daily temperature model (*Input 3*). This step is somewhat more complicated than step 3 because temperature may assume a given value on two occasions during the year—once in the first part of the year (= *before* the hottest day of the year) and again in the second (= *after* the hottest day of the year). To circumvent this ambiguity, the model assumes a pattern of temperature variation with monotonically rising temperatures in the spring and falling temperatures in autumn. The model, therefore, assigns the first solution (spring date) to the initial $\delta^{18}O_{carb}$ sample. This procedure continues until the maximum temperature (minimum $\delta^{18}O_{carb}$ value) is reached, at which point the two solutions are closest to each other in time. The

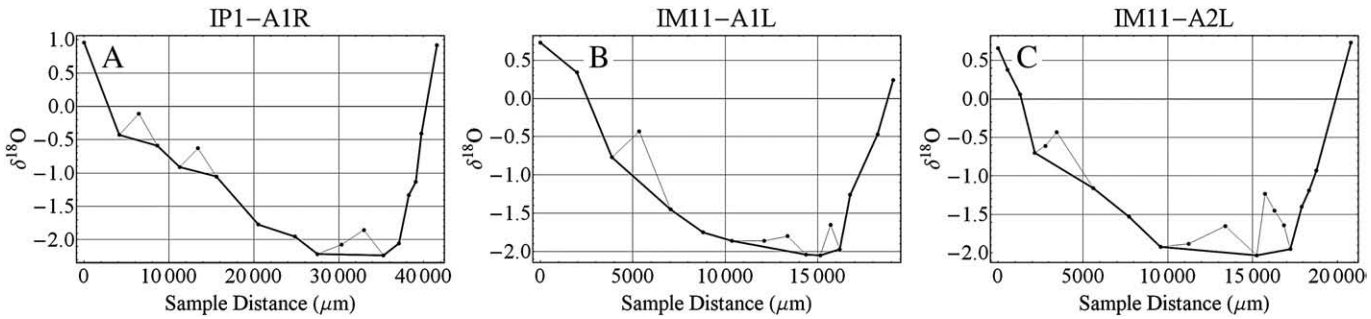

Fig. 3. $\delta^{18}O_{carb}$ versus distance data from the three specimens used in this study. Dots define the original complete data sets (see Appendix A). The bold lines connect samples used to reconstruct doubly monotonic profiles. See text for discussion.

model then assigns a date to the maximum temperature by using the average of these two solutions (spring and autumn). Finally, the remaining temperatures are assigned dates, all of which are after the hottest day of the year. Recall that distance data (cumulative distance between sample holes) is part of *Input 1*. Therefore, on completion of Step 4, we have *N* sets of monotonically increasing distance versus date data sets, with as many points in each set as in the culled $\delta^{18}O_{carb}$ versus distance data set.

In Step 5, a monotonic spline is fit to each of the distance versus time data sets. This curve fitting procedure results in a continuous monotonic function that passes through all of the points in each of the *N* distance versus date data sets. Additional details of the monotonic cubic spline can be found in Appendix B. We use this spline function for several reasons. First, practical considerations usually limit the number of samples in an isotopic profile to between 10 and 20 samples per year and the assumption of constant growth rate (equivalent to linear interpolation) between points is unrealistic (Goodwin et al., 2001). However, given enough $\delta^{18}O_{carb}$ samples, the results obtained using linear interpolation would converge on those obtained using the monotonic cubic spline. Second, because $\delta^{18}O_{carb}$ values represent actual observations on the distance versus time curve, a low-order polynomial fit with a least-squares technique would likely fail to incorporate all of the observations. A spline function, on the other hand, passes through each point in the distance versus date data set, thereby, preserving all of the observed data. Finally, unlike a monotonic cubic spline, a simple cubic spline or a high-order polynomial, while also passing through all of the observed points, can produce intervals with negative slopes. This would imply a biologically impossible scenario where distance along the sampled profile decreases through time (but see Lutz and Rhoads, 1980). The monotonic cubic spline produces a function consistent with clam growth, where new shell material is added to the commissure.

Next, we evaluate the first derivative of the *N* distance versus time functions, which represents the growth rate as a function of time—the growth function (Step 6; Fig. 1). This step results in *N* growth functions derived from the initial $\delta^{18}O_{carb}$ versus distance data set.

Finally, in Step 7, we calculate a moving average for each of the resampled growth functions. We use a 28-day window width to calculate the moving average because it is often difficult to assign calendar dates to tidal increments with a precision greater than ± one fortnight (Koike, 1980; Goodwin et al., 2001). We then calculate an overall average function from the 50 000 smoothed growth functions. The advantage of Step 7 is that, not only does it generate an average growth function, but it also results in an uncertainty envelope. One could argue that the resampling procedure (Step 2) is unnecessary because the average growth function, which is based on a large number of resampled profiles, converges on the growth function that would be obtained by fitting a monotonic cubic spline to the original $\delta^{18}O_{carb}$ versus distance data set. However, without multiple growth functions it would be extremely difficult to evaluate the variability of the modeled growth function.

3. Results

Model output from the analyses of the $\delta^{18}O_{carb}$ versus distance data sets from the three specimens examined in this study are shown Fig. 4 and Table 1. Fig. 4A–C show the average predicted increment width (PIW) profiles with one standard deviation envelopes for IP1-A1R, IM11-A1L, and IM11-A2L, respectively. The profiles are based on the 50 000 PIW values for each respective day of the year. For comparison purposes, Fig. 4D–E show measured increment width (MIW) profiles with a 28-day moving maxima and minima from IP1-A1R, IM11-A1L, and IM11-A2L, respectively. For detailed discussion of these MIW profiles see Goodwin et al. (2003) (IP1-A1R) and Goodwin et al. (2001) (IM11-A1L and IM11-A2L). Table 1 shows a slightly different set of data derived from the model output. It presents the average and standard deviations of *dates* and/or *magnitudes* of specific features in the PIW profiles. For example, the average first day of growth from the 50 000 PIW profiles was 41 ± 5. Corresponding values from the MIW profiles are also given. (Note: the data in Table 1 cannot be read from Fig. 4A–C.).

Several general patterns emerge from these data. The model results suggest that, for each specimen, little or no growth occurred during the first part of the year (Fig. 4A–C). The first day of growth was between Julian day 41 ± 5 and 56 ± 5 and the first day in which growth exceeded 1 μm was between 54 ± 5 an 59 ± 5 (Table 1). Similarly, growth halted

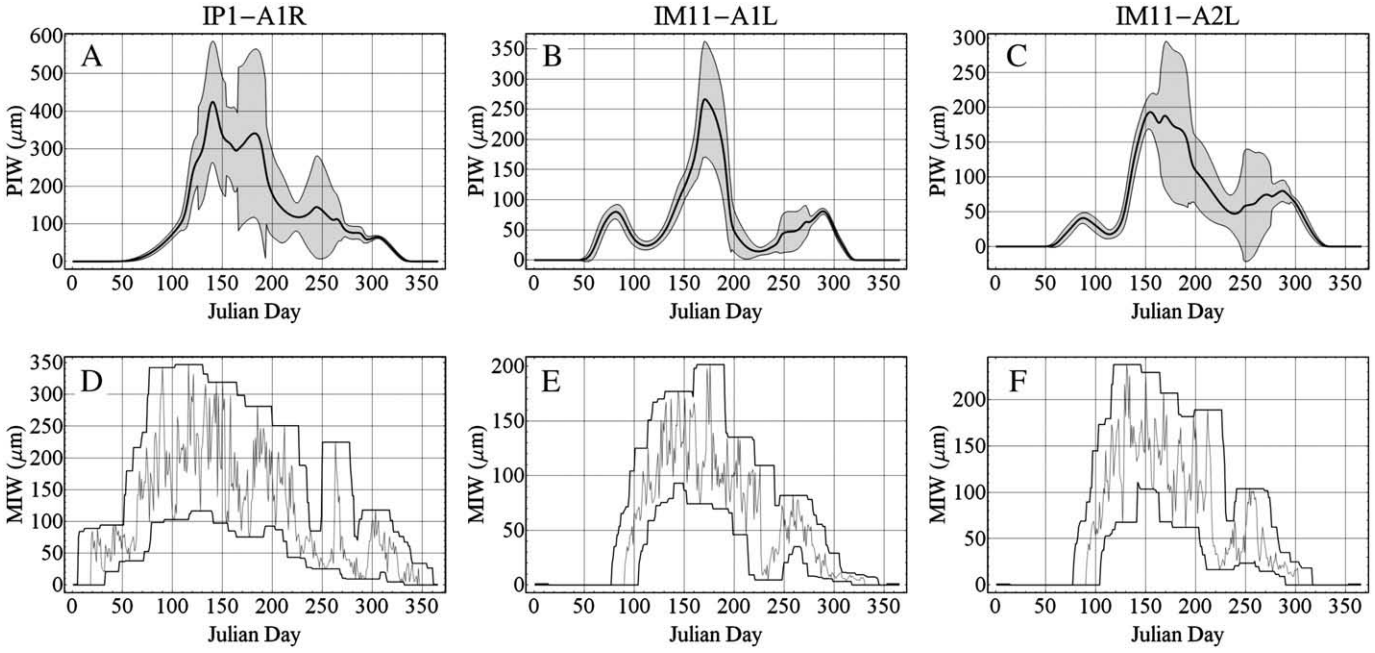

Fig. 4. Modeled and observed growth functions from the three specimens used in this study. (A–C) Modeled growth functions from IP1-A1R, IM11-A1L, and IM11-A2L, respectively. Bold lines are averages of the 50 000 smoothed growth functions. Shaded areas show one standard deviation envelopes. PIW = Predicted Increment Widths. (D–E) Observed increment width profiles from IP1-A1R, IM11-A1L, and IM11-A2L, respectively. Bounding lines show 28-day moving maximum and minimum. MIW = Measured Increment Widths.

Table 1
Comparison of model output and observed aspects of growth functions from the three specimens examined in this study.

Growth function characteristic	IP1-A1R		IM11-A1L		IM11-A2L	
	Modeled	Observed	Modeled	Observed	Modeled	Observed
First day of growth[a]	41 ± 5 (54 ± 5)[b]	19	53 ± 5 (54 ± 5)	91	56 ± 5 (59 ± 5)	91
Last day of growth[a]	336 ± 3 (334 ± 3)	346	320 ± 2 (318 ± 2)	330	331 ± 3 (328 ± 3)	302[c]
Duration of growth[a]	296 (280)	328	268 (265)	240	276 (270)	212
Date of maximum growth[a]	153 ± 20	116	171 ± 10	176	171 ± 29	131
Maximum daily growth (μm)	466 ± 260	347	278 ± 96	201	242 ± 101	238
Temp. on max. growth day (°C)	25 ± 2	NA	27 ± 1	NA	26 ± 2	NA

[a]Julian day.
[b]First value is non-zero growth; second value is growth >1 μm.
[c]0.82 mm from commissure. See Goodwin et al. (2001) for discussion.

before the last day of the year. The last day of growth was between 320 ± 2 and 336 ± 3 and the last day with growth greater than 1 μm was between 318 ± 2 and 334 ± 3 (Table 1). The data suggest that these specimens did not grow throughout the year, but rather deposited shell material in the spring, summer, and fall, and shutdown during the coldest winter months. This is similar to the pattern observed in the MIW profiles. If *C. cortezi* grew throughout the year, we would expect ~352 increments—the number of lunar days in one solar year. However, only 328, 240, and 212 increments were observed in IP1-A1R, IM11-A1L, and IM11-A2L, respectively (Table 1). Furthermore, shell deposition in IM11-A1L and IM11-A2L, which was temporally calibrated by Goodwin et al. (2001), began in late March or early April and ended in late November or early December.

The maximum predicted increment widths are similar to the measured increment widths (Fig. 4 and Table 1). In each case, the maximum MIW is within one standard deviation of the maximum PIW (Table 1). The maximum PIW and MIW from IP1-A1R are larger than those from either of the other specimens (Table 1). That IP1-A1R has the largest increments is expected because it was the ontogenetically youngest specimen and therefore would have had the highest growth rate (Jones et al., 1989).

Similarly, the reconstructed growth function from IP1-A1R suggests it grew more throughout the year than either of the IM11 shells. Fig. 5 shows all three modeled growth functions. The area under each curve represents the total linear growth between the first and last $\delta^{18}O_{carb}$ samples. Integration of these functions shows that IP1-A1R grew over 41 mm, whereas IM11-A1L and IM11-A2L grew approximately 19 and 21 mm, respectively (see Fig. 3; Appendix A). Again, this is not surprising because IP1-A1R was younger and therefore likely grew faster.

The shapes of the three modeled profiles are also broadly similar (Fig. 4A–C). In each case, the beginning of the profile is characterized by zero growth. Following the initiation of shell deposition, growth rates increase rapidly. In IP1-A1R, this pattern continues until the maximum growth rate is reached. In the other shells, the increase in growth rate is not monotonic, but is characterized by a pronounced pulse of growth centered around Julian day 80 followed by rapidly increasing growth rates. After the maximum predicted growth rates, which occurs in the first half of the year in all three profiles, the growth rate decreases gradually. This pattern is best seen in IP1-A1R and IM11-A2L (Fig. 4A and C). In IM11-A1L, however, growth decreases rapidly to a minimum near Julian day 225 (Fig. 4B). A similar, albeit less pronounced, local minimum is seen in IM11-A2L predicted increment width profile (~Julian day 240; Fig. 4C). In each of the IM11 shells, growth rates then rebound to values around 80 μm between Julian 280 and 290. An increase in PIW is also present around Julian day 240 in the IP1-A1R profile, although it is not as distinct. Finally, predicted growth rates in all the shells declines to zero around Julian day 325.

The measured increment width profiles show a similar pattern (Fig. 4D–F). Following the initiation of growth, increment widths increase rapidly in all three specimens. After deposition of the widest increments, the profiles are characterized by gradually declining widths. This pattern is interrupted by an abrupt decrease in increment widths, which is most clearly shown by the IM11 shells (Fig. 4E and F). This interval with narrow increments is followed by a relatively short-lived increase and then a gradual decline in all three specimens. The latest increments counted from each specimen are very narrow and were the last increments formed during their respective years of growth.

The one standard deviation envelopes about the average predicted increment width profiles show several consistent patterns (Fig. 4A–C). First, the highest standard deviations are generally associated with the largest increments. Second, the narrowest predicted increments have the lowest standard deviations. Third, the interval of rapidly increasing PIWs prior to the maximum PIW is characterized by relatively low standard deviations. Finally, there are two intervals characterized by large standard deviations. The first, mentioned above, coincides with the maximum PIWs. The second is associated the final interval of increasing widths (Fig. 4A–C).

4. Discussion

The preceding section illustrates the overall similarity between the predicted increment width profiles and the measured increment width profiles. In particular, the modeled growth profiles provide good estimates of the timing of initiation as well as cessation of growth, the duration of growth, and the maximum growth rate (Table 1). Furthermore, the shape of the modeled intra-annual growth profiles generally reflects the observed growth pattern (Fig. 4).

4.1. Modeled versus observed growth functions

The most obvious difference between the predicted and measured profiles is that the modeled growth functions are relatively smooth, whereas the measured profiles show significant high-frequency variation associated with the tidal cycle (Fig. 4). Using data from IM11-A2L, Schöne et al. (2002b) showed that this high-frequency variation can be filtered from the MIW profile. The result is a filtered growth curve that is virtually identical to our modeled PIW profile from the same specimen (compare our Fig. 4 with Fig. 3d from Schöne et al., 2002b). Both growth curves show a rapid increase in growth rate around Julian day 100, maximum increment widths of approximately 175 μm at day 150, a decline to narrow increments (~50 μm) around

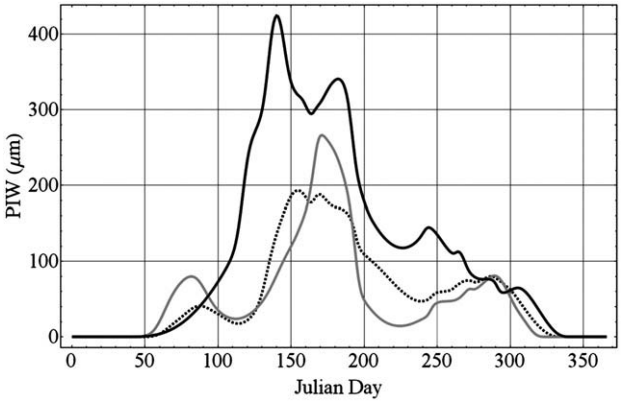

Fig. 5. Modeled predicted increment widths (PIW) versus Julian day for the three specimens. IP1-A1R: black line; IM11-A1L: grey line; IM11-A2L: dotted line.

day 250, a short-lived increase to a local maximum prior to day 300, and finally a cessation of growth prior to day 350. The coincidence of these independently derived growth functions (one based on our modeling procedure and the other derived directly from measured increment widths) provides further evidence that our modeling approach provides reliable estimates of the true intra-annual pattern of growth.

There is, however, one significant difference between the growth function from the Schöne et al. (2002b) analysis and the one obtained here, namely the initial pulse of growth on the modeled growth function around Julian day 80 (Fig. 4C). This interval of growth is not present on the Schöne et al. (2002b) growth function, despite the fact they are derived from the same shell. Recall that a similar growth pulse is shown on the PIW profile from IM11-A1L (Fig. 4B). What, then, is responsible for this apparent pulse of growth in the modeled profiles?

The original $\delta^{18}O_{carb}$ versus distance data from IM11-A1L and IM11-A2L are shown in Fig. 3B and C, and Appendix A. The $\delta^{18}O_{carb}$ samples define one complete cycle of isotopic variation—from one positive peak to the next. Using a temporally calibrated daily increment width profile, Goodwin et al. (2001) assigned calendar dates to the $\delta^{18}O_{carb}$ samples in both profiles. In each case, dates were assigned to all but the first two $\delta^{18}O_{carb}$ samples. These undated samples were separated from the remaining samples by a winter growth break (see Goodwin et al., 2001 for discussion), and therefore were taken from the end of the second year of growth, whereas the remainder of the samples were taken from the third. These samples, therefore, were collected from different years of growth separated by a winter growth break. Inclusion of the undated samples in the $\delta^{18}O_{carb}$ versus distance data set likely forces the model to incorporate the latest growth from the previous year into the PIW profile, resulting in the small local peaks centered around Julian day 80 (Fig. 4B and C). The PIW profile from IP1-A1R does not show this initial pulse of growth (Fig. 4A), suggesting all of the $\delta^{18}O_{carb}$ samples were deposited during the same year (Fig. 3A).

These data highlight the fact that, ideally, only samples deposited in a single year of growth should be included in the original $\delta^{18}O_{carb}$ versus distance data set as part of *Input 1*. However, in the absence of dated $\delta^{18}O_{carb}$ samples, as would be the case when working with fossils or specimens with equivocal increments, we would input $\delta^{18}O_{carb}$ versus distance data that defines a complete peak-to-peak isotopic cycle. These observations suggest our model is somewhat sensitive to the initial choice of $\delta^{18}O_{carb}$ input to the model.

4.2. Model sensitivity to changes of Input 1

To evaluate the effect of using different samples as part of *Input 1*, we compared modeled growth functions from three different analyses of the original $\delta^{18}O_{carb}$ versus distance data set from IM11-A1L (Fig. 3B, Appendix A). In each model run, we selected a different set of $\delta^{18}O_{carb}$ values to construct a new $\delta^{18}O_{carb}$ versus distance profile (Appendix A). The first run used the values selected to define the original doubly monotonic $\delta^{18}O_{carb}$ versus distance profile shown in Fig. 3B. The other two $\delta^{18}O_{carb}$ versus distance profiles were also doubly monotonic, but they were defined using different $\delta^{18}O_{carb}$ values. For example, rather than retaining the first three points and then discarding the forth, as is shown in Fig. 3B, we retained the first two points, discarded the third and retained the forth, etc. In this way, three different doubly monotonic $\delta^{18}O_{carb}$ versus distance data sets were constructed (Appendix A). There were, however, intervals in which the same points were retained in each $\delta^{18}O_{carb}$ versus distance data set. For example, $\delta^{18}O_{carb}$ samples 1, 2, 5, 6, 10, 14–16 were used in all three model runs (Appendix A).

The PIW profiles based on three different $\delta^{18}O_{carb}$ versus distance data sets are shown in Fig. 6. The overall shape of the growth functions is very similar: each is characterized by three distinct pulses of growth. Because $\delta^{18}O_{carb}$ samples one and two were retained in all three $\delta^{18}O_{carb}$ versus distance data sets, the first peak represents growth from the previous year (see above). Together the second and third pulses of growth are similar to MIW profiles from IM11-A1L and the filtered growth profile of Schöne et al. (2002b).

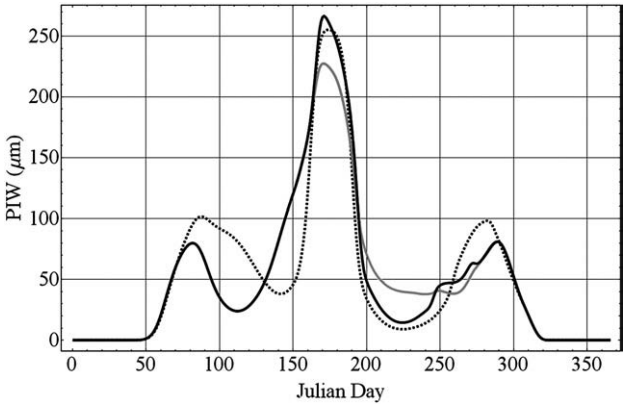

Fig. 6. Predicted increment width profiles from IM11-A1L based on three different $\delta^{18}O_{carb}$ versus distance data sets. Run 1: black line; Run 2: grey line; Run 3; dotted line. See Appendix A and text for discussion.

These modeled profiles suggest that, regardless of which points are retained from the original $\delta^{18}O_{carb}$ versus distance data set, our model produces consistent results. Some of the similarity certainly reflects the fact that the three doubly monotonic $\delta^{18}O_{carb}$ versus distance data sets contain many of the same individual $\delta^{18}O_{carb}$ samples (Appendix A). However, the similarity of these profiles also suggests that the model will produce reliable results regardless of where samples are collected from shell. This is an important result because it means that no special sampling protocol is required.

4.3. Reconstructing optimal growth temperatures

In addition to reconstructing aspects of intra-annual growth, the PIW profiles can be used to identify optimal growth temperatures. In Fig. 7A the PIW profiles from IP1-A1R, IM11-A1L and IM11-A2L have been scaled by their respective maximum growth rates so that increments widths range between zero and one. To illustrate the relationship between PIWs and temperature, the smooth daily temperature model (*Input 3*) is also shown. Notice that the growth rates in all three profiles increases dramatically between Julian day 110 and 170. This interval of rapidly increasing predicted increment widths occurred when temperatures were between 20 and 27 °C. Similarly, maximum growth rates (Julian day 140 and 170) correspond to temperatures between 23 and 27 °C. When temperatures rise above 27 °C growth rates decline and when they rise above 29 °C growth rates decline precipitously. At the warmest temperatures of the year (~31 °C around Julian day 225), growth rates decline to a temporary minimum. This phenomenon most clearly seen in profiles from IM11-A1L and IM11-A2L although a local minimum is also present in the PIW profile from the ontogenetically younger specimen IP1-A1R (Fig. 7A). As temperatures begin to decline in autumn, growth rates increase again. When temperature is between 27 and 20 °C the IM11 shells show a pulse of growth. Finally, as temperatures cool below ~19 °C growth rates decline to zero.

The relationship between temperature and predicted increment widths is shown slightly differently in Fig. 7B. Here, normalized PIWs are plotted as a function of temperature. This graph suggests that in *C.* (*C.*) *cortezi* little shell deposition occurs when temperatures are below ~15 °C. Growth rate increases dramatically when water temperatures rise above approximately 20 °C, maximum growth rates occur between 23 and 27 °C, and little shell deposition occurs when temperatures are above ~30 °C.

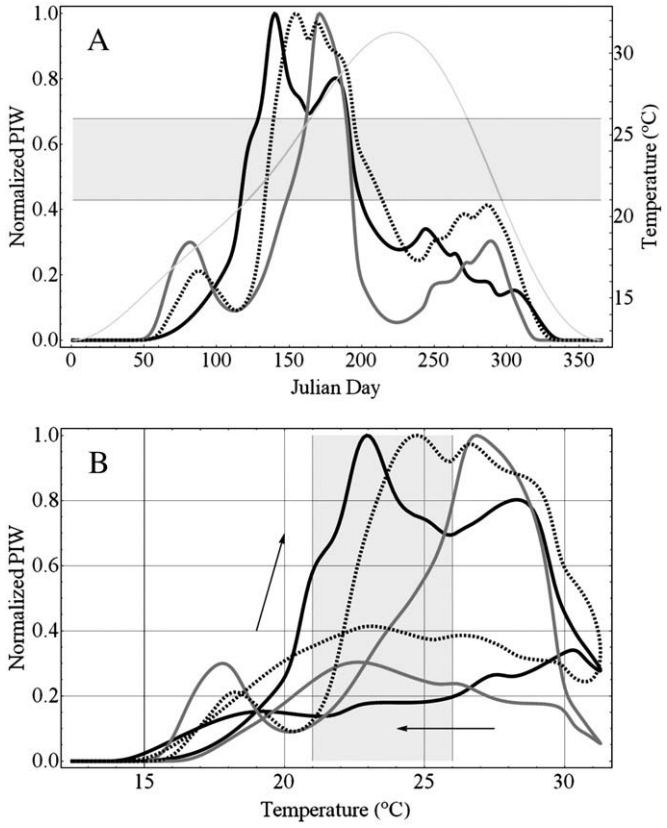

Fig. 7. Scaled predicted increment width profiles from the three shells analyzed in this study. (A) Scaled PIW profiles as a function of time. The smooth daily temperature model (*Input 3*) is also shown. (B) Scaled PIW profiles as a function of temperature. IP1-A1R: black line; IM11-A1L: grey line; IM11-A2L: dotted line. In each panel the shaded area shows independently derived optimal growth temperatures. See text for discussion.

Optimal growth temperatures can also be estimated using the 50 000 resampled profiles. Furthermore, whereas only a single estimate of optimal growth temperatures can be derived from the average PIW profile, the 50 000 resampled profiles can also be used to calculate its variance. In this case, the estimated optimal growth temperatures range from 25 ± 2 to 27 ± 1 °C (Table 1). These estimates were obtained by calculating the average of the daily temperatures on the day of maximum growth from each of the 50 000 resampled profiles from each shell.

These observations agree well with two independently derived estimates of optimal growth temperatures for *C* (*C.*) *cortezi*. Goodwin et al. (2001) suggested that growth rates were fastest when temperatures were between 23 and 26 °C, whereas Schöne et al. (2002a) postulated that optimal growth occurred between 21 and 24 °C. In Fig. 7A and B the combined optimal growth range from Goodwin et al. (2001) and Schöne et al. (2002a) (21 and 26 °C) is shown in the shaded area. The optimal growth temperatures derived from the PIW profiles are 23 to 27 °C, and 25 ± 2 to 27 ± 1 °C from the 50 000 resampled profiles. The overlap of these independent estimates suggests our modeling procedure produces reliable estimates of optimal growth temperatures.

4.4. Applications of the model

That the MoGroFunGen model can identify optimal growth temperatures is particularly significant. Using only a $\delta^{18}O_{carb}$ versus distance data set, a static $\delta^{18}O_{water}$, and a temperature model, MoGroFunGen successfully reconstructs when and under what conditions the clams grow fastest. Recall that no direct measures of growth rates are used to construct the predicted increment width profiles. This model, therefore, is a "value-added" analytical procedure: it can be easily applied to isotopic profiles to generate additional ecological data at little or no additional expense.

Furthermore, model output may also be used to identify the influence of factors other than temperature that control intra-annual growth. Notice that temperatures are in the optimal range twice during the year, once in the spring and again in the fall (Fig. 7). If temperature were the sole factor governing growth, PIWs during these two intervals should be the same. However, growth rates are much higher in the first part of the year. This observation suggests that a factor other than temperature influenced growth. The next step then would be to correlate the PIW profiles with time-series of other environmental factors to determine how they affect growth rates. And, in fact, Schöne et al. (2002b) and Schöne et al. (2006) suggest that, in *C* (*C.*) *cortezi*, intra-annual growth rates are correlated with phytoplankton abundance, which suggests nutrient concentrations also affect growth rates.

Documenting optimal growth temperatures can be a useful tool in modern natural history studies. For example, reconstructed optimal growth temperatures can be compared across a taxon's geographic range to identify regional differences in environmental preferences (Jones and Quitmyer, 1996). Optimal growth temperatures could also be combined with oceanographic models to predict how different species will respond to environmental change.

Application of the MoGroFunGen model to fossils may also yield valuable paleoenvironmental, paleoecological, and evolutionary information. To do this, of course, requires knowledge of intra-annual temperature variation as well as the isotopic composition of the water. However, in most circumstances, unless using independent paleoenvironmental proxies, these parameters are unknown. Nevertheless, by using the same set of realistic environmental parameters, predicted increment width profiles could easily be compared within and across evolutionary lineages in space and/or time. These data, in turn, may be used to document how environmental tolerances change within a lineage or to determine how environmental conditions affect the growth of contemporaneous species.

Finally, while MoGroFunGen was originally conceived to reconstruct the intra-annual growth of bivalve molluscs, there is no reason why the modeling approach proposed here could not be applied to other archives with accretionary growth (biogenic or otherwise). This method, therefore, may become an important tool in the study of growth rates in general.

5. Conclusions

Here we present a numerical model (MoGroFunGen: Mollusk Growth Function Generator) that relates linear growth and time using stable oxygen isotopes to reconstruct intra-annual growth rates in bivalve molluscs. We applied our model to three shells collected in the northern Gulf of California. From these analyses the following conclusions are drawn:

1. Many aspects of the predicted increment width profiles closely match observed patterns of intra-annual growth. These similarities include the dates of initiation and cessation of growth, the duration of growth, the date of maximum growth, and the maximum daily increment width.
2. The overall shape of the predicted increment width profiles is similar to the observed pattern of intra-annual growth. Little or no shell deposition occurs in the earliest part of the year. The widest increments are deposited in the spring. Increment widths decrease dramatically during the hottest part of the year. When temperatures fall in the autumn widths partially rebound and then decrease to zero in the last part of the year.
3. Only samples deposited in a single year of growth should be included in the original $\delta^{18}O_{carb}$ versus distance data set. However, in

the absence *a priori* knowledge of growth patterns, the $\delta^{18}O_{carb}$ versus distance data should be taken from a single isotopic cycle. The model is somewhat sensitive to the initial choice of $\delta^{18}O_{carb}$ samples input to the model.

4. MoGroFunGen is relatively insensitive, however, to which points in the original $\delta^{18}O_{carb}$ versus distance data set are used to define *Input 1*. This observation suggests that no special sampling collection protocol is required when initially drilling a specimen.
5. The model provides reasonable estimates of optimal growth temperatures. This finding is especially significant because estimated optimal growth temperature are derived solely from $\delta^{18}O_{carb}$ versus distance data, a static $\delta^{18}O$ water value, and a temperature model, without any *a priori* knowledge of growth rates. Furthermore, the predicted increment width profile can easily be correlated with records of environmental variation other than temperature to determine how they affect growth rates.
6. The MoGroFunGen model may be a valuable new source of ecological and paleoecological information on the growth of bivalve mollusks as well as other organisms/archives with accretionary skeletons.

Acknowledgments

We thank Peter D. Roopnarine and David P. Gillikin for insightful discussions of the model. Thanks also to David L. Dettman, Karl W. Flessa, and Bernd R. Schöne for their work on the initial sclerochronological analyses of the specimens used in this study. This paper greatly benefited from the thoughtful reviews by Thierry Corrège, Donna Surge and an anonymous reviewer. This study was funded by support from the Howard Hughes Medical Institute, the Anderson Endowment of Denison University, and the Michelle Tolela Myers New Faculty Start-Up Program (Denison University).

Appendix A. $\delta^{18}O_{carb}$ vs. distance data

$\delta^{18}O_{carb}$ versus distance data from the three specimens examined in this study. The superscripted numbers following the oxygen isotope values from IM11-A1L represent the values retained when constructing three different versions of *Input 1* (see Section 4.2).

Sample No.	IP1-A1R		IM11-A1L		IM11-A2L	
	$\delta^{18}O$	Dist.[a]	$\delta^{18}O$	Dist.[a]	$\delta^{18}O$	Dist.[a]
1	0.96	0	$0.73^{1,2,3}$	0	0.66	0
2	−0.43	4139	$0.34^{1,2,3}$	1972	0.38	556
3	−0.11	6456	$-0.77^{1,2}$	3873	0.06	1296
4	−0.59	8609	-0.43^{3}	5352	−0.70	2161
5	−0.91	11258	$-1.45^{1,2,3}$	7042	−0.61	2778
6	−0.63	13410	$-1.75^{1,2,3}$	8803	−0.43	3457
7	−1.05	15562	$-1.86^{1,3}$	10352	−1.16	5617
8	−1.77	20529	-1.86^{2}	12113	−1.53	7716
9	−1.95	24834	−1.80	13380	−1.92	9568
10	−2.21	27483	$-2.04^{1,2,3}$	14366	−1.88	11235
11	−2.07	30298	$-2.05^{1,2}$	15141	−1.65	13395
12	−1.85	32947	-1.65^{2}	15704	−2.03	15247
13	−2.23	35264	$-1.97^{1,3}$	16197	−1.23	15741
14	−2.05	37086	$-1.26^{1,2,3}$	16761	−1.45	16296
15	−1.33	38245	$-0.47^{1,2,3}$	18239	−1.64	16852
16	−1.13	39072	$0.24^{1,2,3}$	19085	−1.95	17222
17	−0.41	39735			−1.40	17901
18	0.92	41556			−1.19	18333
19					−0.93	18765
20					0.73	20802

[a]μm.

Appendix B. Monotonic cubic spline

The monotone cubic spline algorithm was adapted from Fritsch and Carlson (1980). We assume the measured doubly monotonic $\delta^{18}O_{carb}$ versus distance data runs through one complete annual growth cycle with shutdown (zero growth rate) at both ends. Let a distance (x) versus time (t) set consist of n points (t_k, x_k) for $k=1,\ldots, n$. The steps leading to a monotone spline are as follows:

1. Define $\Delta_k=(x_{k+1}-x_k)/(t_{k+1}-t_k)$ for $k=1,\ldots,n-1$.
2. Initialize $m_k=(\Delta_{k-1}+\Delta_k)/2$ for $k=2,\ldots, n-1$ and $m_1=m_n=0$.
3. If $\Delta_k=0$ then set $m_{k+1}=0$, for $k=1,\ldots, n-1$.
4. If $\sqrt{m_k^2+m_{k+1}^2}>3\Delta_k$ then set:

$$m_k = 3\Delta_k m_k / \sqrt{m_k^2+m_{k+1}^2}$$

$$m_{k+1} = 3\Delta_k m_{k+1} / \sqrt{m_k^2+m_{k+1}^2},$$

for $k=1,\ldots, n-1$.

5. The cubic spline consists of pieces such that for $t_k \le t \le t_{k+1}$, $x = x_k h_{00}(z)+x_{k+1}h_{01}(z)+hm_k h_{10}(z)+hm_{k+1}h_{11}(z)$, where $h=t_{k+1}-t_k$, $z=(t-t_k)/h$, and the cubic Hermite basis functions are:

$$h_{00}(z) = 2z^3-3z^2+1$$
$$h_{01}(z) = -2z^3+3z^2$$
$$h_{10}(z) = z^3-2z^2+z$$
$$h_{11}(z) = z^3-z^2.$$

References

Coe, W., 1948. Nutrition, environmental conditions, and growth of marine bivalve mollusks. J. Mar. Res. 7 (3), 586–601.
De Ridder, F., Pintelon, R., Schoukens, J., Gillikin, D.P., André, L., Baeyens, W., de Brauwere, A., Dehairs, F., 2004. Decoding nonlinear growth rates in biogenic environmental archives. Geochem. Geophys. Geosyst. 5, Q12015.
De Ridder, F., de Brauwere, A., Pintelon, R., Schoukens, J., Dehairs, F., Baeyens, W., Wilkinson, B.H., 2007. Comment on: paleoclimatic inference from stable isotope profiles of accretionary biogenic hardparts—a quantitative approach to the evaluation of incomplete data, by Wilkinson, B.H., Ivany, L.C., 2002. Palaeogeogr. Palaeocl. Palaeoecol. 185, 95–114 Palaeogeography Palaeoclimatology Palaeoecology, 248(3–4):473–476.
Elliot, M., deMenocal, P., Linsley, B., Howe, S., 2003. Environmental controls on the stable isotopic composition of *Mercenaria mercenaria*: potential application to paleoenvironmental studies. Geochem. Geophys. Geosyst. 4.
Fritsch, F.N., Carlson, R.E., 1980. Monotone piecewise cubic interpolation. SIAM J. Numer. Anal. 17, 238–246.
Goodwin, D.H., Flessa, K.W., Schöne, B.R., Dettman, D.L., 2001. Cross-calibration of daily growth increments, stable isotope variation, and temperature in the gulf of California bivalve mollusk *Chione cortezi*: implications for paleoenvironmental analysis. Palaios 16 (4), 387–398.
Goodwin, D.H., Schöne, B.R., Dettman, D.L., 2003. Resolution and fidelity of oxygen isotopes as paleotemperature proxies in bivalve mollusk shells: models and observations. Palaios 18 (2), 110–125.
Goodwin, D.H., Anderson, L.C., Roopnarine, P.D., 2008a. Evolutionary origins of novel conchologic growth patterns in tropical American corbulid Bivalves. Evol. Dev. 10, 642–656.
Goodwin, D.H., Paul, P., Wissink, C.L., 2008b. Modeling intra-annual growth of freshwater mussels. GSA Abstracts with Programs 40 (6), 439.
Grossman, E., Ku, T., 1986. Oxygen and carbon isotope fractionation in biogenic aragonite: temperature effects. Chem. Geol. 59 (1), 59–74.
Ivany, L.C., Wilkinson, B.H., Jones, D., 2003. Using stable isotopic data to resolve rate and duration of growth throughout ontogeny: an example from the surf clam, *spisula solidissima*. Palaios 18, 126–137.
Jones, D., Gould, S., 1999. Direct measurement of age in fossil Gryphaea: the solution to a classic problem in heterochrony. Paleobiology 25 (2), 158–187.
Jones, D., Quitmyer, I., 1996. Marking time with bivalve shells: oxygen isotopes and season of annual increment formation. Palaios 11, 340–346.
Jones, D., Arthur, M., Allard, D., 1989. Sclerochronological records of temperature and growth from shells of *Mercenaria mercenaria* from Narragansett Bay, Rhode Island. Mar. Biol. 102 (2), 225–234.
Koike, H., 1980. Seasonal dating by growth line counting of the bivalve, *Meretrix lusoria*. University of Tokyo Bulletin, 18, pp. 1–120.
Lutz, R., Rhoads, D., 1980. Growth patterns in the molluscan shell: an overview. In: Rhoads, D.C., Lutz, R.A. (Eds.), Skeletal Growth of Aquatic Organisms: Biological Records of Environmental Change. Plenum Press, pp. 203–254.
Ohno, T., 1989. Paleotidal characteristics determined by micro-growth patterns in bivalves. Palaeontology 32 (Part 2), 237–263.
Richardson, C., 2001. Molluscs as archives of environmental change. Oceanogr. Mar. Biol.: Ann. Rev. 39, 103–164.
Richardson, C., Crisp, D., Runham, N., 1981. Factors influencing shell deposition during a tidal cycle in the intertidal bivalve *Cerastoderma Edule*. J. Mar. Biol. Assoc. U. K. 61 (2), 465–476.

Sato, S., 1995. Spawning periodicity and shell microgrowth patterns of the venerid bivalve *Phacosoma japonicum* (Reeve, 1850). Veliger 38 (1), 61–72.

Schöne, B.R., Goodwin, D.H., Flessa, K.W., Dettman, D.L., Roopnarine, P.D., 2002a. Sclerochronology and growth of the bivalve mollusks *Chione (Chionista) fluctifraga* and *C. (Chionista) cortezi* in the northern Gulf of California, Mexico. Veliger 45 (1), 45–54.

Schöne, B.R., Lega, J., Flessa, K.W., Goodwin, D.H., Dettman, D.L., 2002b. Reconstructing daily temperatures from growth rates of the intertidal bivalve mollusk *Chione cortezi* (northern Gulf of California, Mexico). Palaeogeogr. Palaeoclimatol. Palaeoecol. 184 (1–2), 131–146.

Schöne, B.R., Flessa, K.W., Dettman, D.L., Goodwin, D.H., 2003. Upstream dams and downstream clams: growth rates of bivalve mollusks unveil impact of river management on estuarine ecosystems (Colorado River Delta, Mexico). Estuar. Coast. Shelf Sci. 58 (4), 715–726.

Schöne, B.R., Rodland, D.L., Fiebig, J., Oschmann, W., Goodwin, D.H., Flessa, K.W., Dettman, D.L., 2006. Reliability of multitaxon, multiproxy reconstructions of environmental conditions from accretionary biogenic skeletons. J. Geol. 114, 267–285.

Wefer, G., Berger, W., 1991. Isotope paleontology: growth and composition of extant calcareous species. Mar. Geol. 100 (1–4), 207–248.

Wilkinson, B., Ivany, L., 2002. Paleoclimatic inference from stable isotope profiles of accretionary biogenic hardparts – a quantitative approach to the evaluation of incomplete data. Palaeogeogr. Palaeoclimatol. Palaeoecol. 185 (1–2), 95–114.